



OPEN Stability analysis of existing tunnels under dynamic loads during excavation of new tunnels

Hao Li¹, Sichun Long^{1✉}, Xiangen Lai², Lijun Kuang³, Jian Zhou³, Mengguang Liao¹ & Chaofeng Zeng¹

Understanding the deformation mechanism and behaviour of adjacent tunnels subjected to dynamic train loads provides vital technical insights for engineering design. This study conducted a detailed analysis and revealed that tunnel excavation significantly affects the stability of adjacent existing tunnels under dynamic loads. First, we developed a dynamic load simulation approach and derived a calculation formula for shield-soil friction. A methodology for analyzing the stress in the surrounding rock of the tunnel was established. Subsequently, the impact of dynamic loads on the stability of existing tunnels was assessed through numerical simulations. Finally, the numerical results were compared with field-measured data to validate the reliability of the research findings. The results indicated that, compared to the condition without train load, the maximum vertical and lateral displacements at the vault of the existing tunnel under dynamic load condition increased by 2.9 mm and 1 mm, respectively, leading to an overall safety and stability coefficient reduction of approximately 0.1. Furthermore, the influence of dynamic loads on the stability of the existing tunnel intensified with increasing train speeds under various load conditions. For train speeds of ≤ 40 km/h, the dynamic load could effectively be considered as a static load. Notably, the surrounding soft rock exhibited a higher degree of stress release compared to the surrounding hard rock. The stresses at the soft-hard rock interface were found to potentially induce damage to the tunnel. In scenarios where new and existing tunnels were in proximity, the dynamic load was incorporated into the entire simulation process, yielding results that closely aligned with actual measurements.

Keywords Dynamic load, Soil friction, Surrounding rock stress, Tunnel stability

The rapid advancement of urban development has led to accelerated construction activities. Ground disturbance during shield tunnelling inevitably affects existing tunnels, leading to structural deformations. To enhance the stability of these structures and facilitate effective subway operations, it is imperative to conduct extensive research regarding the impact of tunnel excavation on the stability of adjacent existing tunnels.

Numerous scholars worldwide have investigated this topic utilizing various methods such as theoretical analysis, numerical simulations, model tests, and others. For example, Liu et al.¹ utilized numerical simulations and three-dimensional (3D) theoretical analyses to develop an improved rotational damage theoretical model. Additionally, they derived an equation for the ultimate support force on excavation surface by considering soil cohesion and gravitational effects. Zhang and Sun² employed both upper bound and quasi-static methods to derive analytical formulas for stability coefficient, thereby leading to a more comprehensive approach for assessing geotechnical slope stability. Lou and Li³ developed a finite element model to evaluate soil displacement and ground settlement during overlapping tunnel excavations. They examined the effects of excavation face pressure and grouting pressure on ground settlement. Zhu et al.⁴ introduced a novel technique for monitoring ground deformation through the integration of synthetic aperture radar (SAR) images from diverse satellite platforms. Ding et al.⁵ performed a numerical analysis to explore how clearance distance and angle between two tunnels in soft soil affect subway deformation, internal lining forces, and adjacent partition areas. Zhou et al.⁶ presented an innovative intelligent model known as the Grey Wolf optimizer-based Random Forest (GWO-RF) model to predict water inflow (WI) in tunnel construction. Zou et al.⁷ optimized assessment method for tunnel face stability by modifying the logarithmic spiral rotation model above the tunnel vault to a semi-elliptical shape. Li et al.⁸ employed a strain-softening constitutive model to analyze the stress distribution, deformation, and

¹School of Earth Sciences and Spatial Information Engineering, Hunan University of Science and Technology, Xiangtan 411201, China. ²China Construction Fifth Engineering Bureau Civil Engineering Co., Ltd, Changsha 410011, China. ³China Construction Fifth Engineering Co., Ltd, Shenzhen 518108, China. ✉email: sclong@hnust.edu.cn

strength of rocks surrounding the deep roadways. Lu et al.⁹ utilized the Mindlin solution in conjunction with the Loganathan formula to examine elastic displacement field in the soil resulting from bulkhead additive thrust, friction force, as well as ground loss between shield and soil through numerical integration.

In recent years, the increase in urban traffic loads has heightened attention on the stress conditions and deformation control challenges faced by underground tunnels under vehicle loads. Long et al.¹⁰ developed a novel method for monitoring the structural health of bridges, which successfully captured the entire process from initial deformation to complete failure. Wang et al.¹¹ examined soil vibration responses around the tunnel under single-train train operations, bidirectional train traffic, and varying tunnel depths. Xiang et al.¹² highlighted challenges in controlling the rock deformation at tunnel base following the removal of prestressing anchors. This operation contributed to ongoing issues of bottom rumble. In conjunction with numerical simulations, they explored the failure mechanism associated with pre-stressed anchor remediation for the bottom rumble in railroad tunnels operated in gently dipping laminar rock under train-induced vibration loads. Li et al.¹³ established a rock experimental system integrating electrical and mechanical components to analyze the patterns of microcurrents generated during rock loading and their microscopic influence mechanisms. Long et al.¹⁴ performed a series of laboratory experiments focused on dynamic deformation and failure in a physical model bridge subjected to sequential loading.

In summary, considerable research has been conducted regarding tunnel underpasses and their interactions with dynamic loads. However, there remains a scarcity of studies directly addressing the dynamic responses of tunnels to such loads. Many computational models for shield tunnels often overlooked the influence of dynamic loads and seldom examined how these loads impact the various contact forces within the models—a crucial factor contributing to the displacement of existing tunnels during shield tunnelling operations. Consequently, there is a pressing need to investigate the implications of dynamic loads on tunnel excavation stability. This study employed FLAC3D finite difference software to simulate the entire process of a newly constructed tunnel being excavated beneath an existing tunnel. Additionally, the subway train load within the existing tunnel was simulated to explore its impact on both tunnel structure and underlying soil during excavation. Finally, simulation results were compared with on-site measurements to validate the reliability of the research findings.

Summary of the work

The subway shield was projected vertically beneath the existing subway, with a clearance distance of 2.8 m and a depth of 24.5 m. The thicknesses of primary support is 25 cm, and the thickness of and secondary lining are measures 25 cm and 30 cm. During interval tunnel construction using the shield method, the maximum train speed within the existing tunnel was 80 km/h, with an operating speed of 60 km/h.

The interval tunnel was located in the Weihe River tertiary order area. The artificial fill underneath consists of powdery clay, while the bedrock consists of medium-thick-thick bedded Cretaceous mud siltstone. The engineering properties of various rock and soil layers exhibited significant variability. The site is characterized by a continuous distribution of the fourth series of strata with a gradual transition between rock and soil masses. The entire tunnel section is located within the medium-weathering muddy siltstone, which features uniform rock distribution with high strength and small deformation. The load-bearing capacity of the strata met design requirements, while the foundation soil was uniform. Figure 1 illustrates the spatial relationship between the new and existing tunnels.

Theoretical analysis

Dynamic load simulation

A metro train load simulation involves multiple factors, such as metro system, track system, and roadbed structure¹⁵. Therefore, it presents a complex system dynamics challenge. The ideal approach for subway train load simulation involves establishing a comprehensive system model that integrates the subway train, track, roadbed, and foundation. Dynamic analysis should consider nonlinear interactions such as wheel-track contact

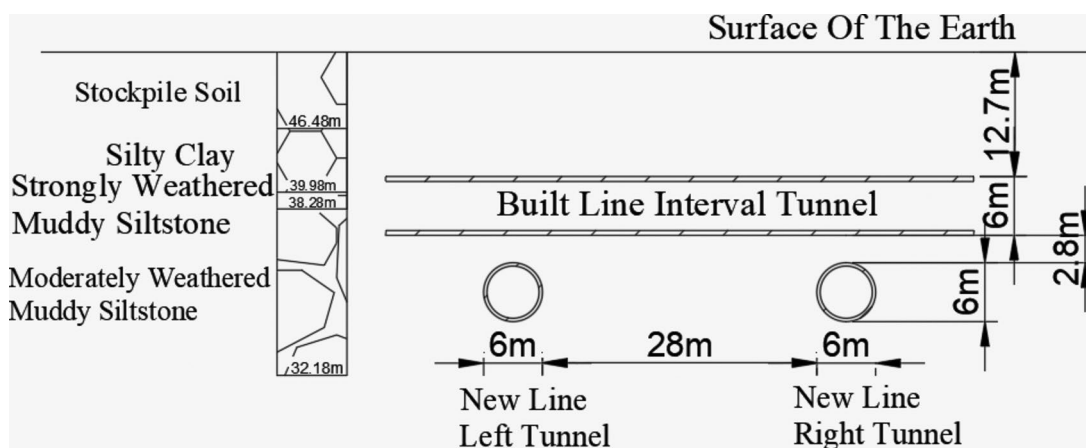


Fig. 1. Schematic diagram illustrating the spatial relationship between the new and existing tunnels.

and collisions. When a subway train travels on the track, the wheel-track contact force is transmitted to the underlying tunnel structure via the track fastener system. Due to the impact of wheels on the track and the track's unevenness, periodic excitation vibrations of certain frequencies are generated. In examining the impact of vibrational forces from subway trains on underlying soil, many scholars have included additional dynamic loads and rail surface wave abrasion effects to accurately model the subway train load^{16–19}. The excitation load can be expressed as follows:

$$F(t) = k_1 k_2 F(t)' = k_1 k_2 (p_0 + p_1 \sin \omega_1 t + p_2 \sin \omega_2 t + p_3 \sin \omega_3 t), \quad (1)$$

where k_1 denotes the superposition coefficient related to neighboring wheels and rails, which typically ranges from 1.2 to 1.7; k_2 signifies the dispersion coefficient concerning rails and sleepers, which generally ranges from 0.6 to 0.9; p_0 represents the static load on the wheels; p_1 , p_2 , and p_3 are the load magnitudes in the high-, medium-, and low-frequency bands of vibration loads generated by subway trains; t denotes the time variable; and ω_1 , ω_2 , and ω_3 are the angular frequency responses to vibrations across these frequency bands.

The design standard for railroad sleeper clarifies that the p_0 is 100 kN, and the spring mass M_0 is 750 kg. Referring to the track unevenness control values, there are $L_1 = 10$ m, $L_2 = 2$ m, and $L_3 = 0.5$ m. The rise corresponding to the circular frequency (ω_i) is α_i , where $\alpha_1 = \alpha_2 = \alpha_3 = 3.5$ mm, $k_1 = 1.7$, and $k_2 = 0.9$.

The numerical simulations analyzed the impact of dynamic loads on the overall stability of the tunnel structure with subway trains operating at speeds of 0, 40, and 80 km/h, respectively.

Formula for shield shell-soil friction

The current method for evaluating shield shell-soil friction, as depicted in Fig. 2a by Yin et al.²⁰, does not account for dynamic loads. As illustrated in Fig. 2b, this study introduced an enhanced friction calculation approach, where variables such as q_e (lateral earth pressure), p_{e1} (top earth pressure), p_{e2} (bottom earth pressure), F_{y1} , F_{y2} and F_{y3} (stress fields from dynamics in each direction), p_1 (lateral earth pressure and effective stress field radially), p_2 (vertical earth pressure and effective stress field radially, r (radius of shield cutter plate), and θ (angle with the horizontal direction) were considered.

The sum of lateral earth pressure q_e , vertical earth pressures p_{e1} , and p_{e2} in the radial direction of the shield represents the magnitude of the support force. The lateral earth pressure q_e is symmetric left and right, and is calculated as follows:

$$q_e = K\gamma [h_N + r(1 - \sin\theta)] + F_{y3}, \quad (2)$$

where K represents the static lateral pressure coefficient of the stratum where the shield is situated, which is typically computed using $K = 1 - \sin\varphi$, where F_{y3} is the lateral stress field calculated from dynamic loads.

Therefore, the lateral earth pressure component force p_1 within the radial unit length of the shield can be calculated as:

$$dp_1 = [K\gamma h_N \cos\theta + K\gamma r(1 - \sin\theta) \cos\theta + F_{y3} \cos\theta] r d\theta, \quad (3)$$

For vertical earth pressure, top and bottom earth pressures are determined by accounting for the self-weight of the shield acting on the bottom soil:

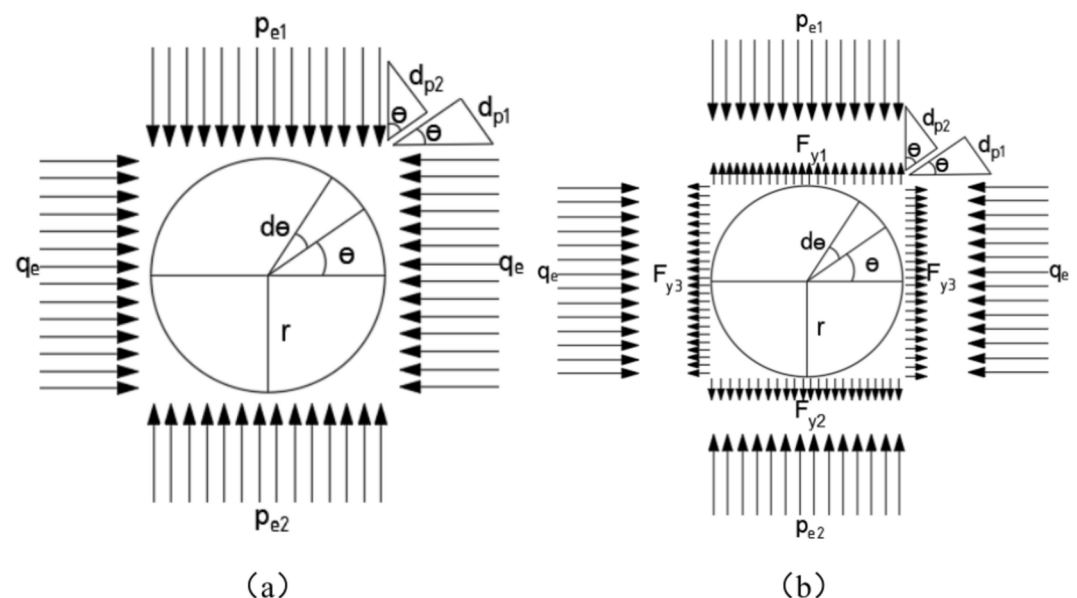


Fig. 2. Schematic diagram of friction calculation formula.

$$p_{e1} = \gamma [h_N + r (1 + \sin\theta)] + F_{y1}, \quad (4)$$

$$p_{e2} = \gamma [h_N + r (1 - \sin\theta)] + \frac{W}{\pi r l_{sh}} + F_{y2}, \quad (5)$$

where F_{y1} is the top stress field calculated from dynamic loads; and F_{y2} is the bottom stress field calculated from dynamic loads.

Therefore, the formulas for calculating the vertical earth pressures resulting from the radial unit length component force of p_2 the shield are as follows:

$$d_{p2 \perp} = \{\gamma(K + 1)[h_N + r(1 - \sin\theta)] + F_{y1}\}rd\theta, \quad (6)$$

$$dp_{2 \overline{r}} = \left\{ \gamma(K + 1)[h_N + r(1 - \sin\theta)] + \frac{W}{\pi r l_{sh}} + F_{y2} \right\}rd\theta, \quad (7)$$

Therefore, the friction of the soil around the shield is calculated as follows:

$$dF_{f1} = \eta (d_{p1} + d_{p2 \perp}) dl_{sh}, \quad (8)$$

$$dF_{f2} = \eta (d_{p1} + d_{p2 \overline{r}}) dl_{sh}, \quad (9)$$

Stress in surrounding rock of existing tunnels

As depicted in Fig. 3, the stress in the surrounding rock was decomposed into two components to ensure isotropy in all directions^{21,22}:

$$\begin{cases} P_z = p + p' \\ P_x = p - p' \end{cases}, \quad (10)$$

where P_x and P_z denotes the lateral and vertical stresses, respectively; and p and p' are decomposed stresses. Solving Eq. (10) yields:

$$\begin{cases} p = \frac{1}{2} (1 + \lambda) p_z \\ p' = \frac{1}{2} (1 - \lambda) p_z \end{cases}, \quad (11)$$

where λ is the natural stress ratio coefficient of the surrounding rock.

According to the theory of elasticity for axisymmetric circular tunnels, when the tunnel is symmetric around the z-axis, the tangential stress $\tau_{\theta r}$ is 0. Consequently, the tangential and radial stresses borne by surrounding rock are both the principal stresses. The tangential and radial stresses in the surrounding rock can be expressed as:

$$\begin{cases} \sigma_{\theta} = P_z \left(1 + \frac{r^2}{R^2} \right) \\ \sigma_r = P_z \left(1 - \frac{r^2}{R^2} \right) \end{cases}. \quad (12)$$

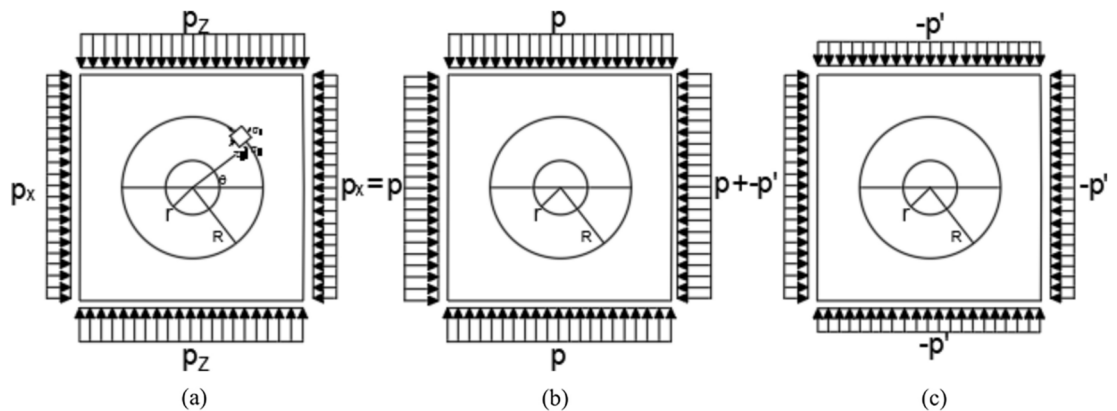


Fig. 3. Schematic diagram of stress decomposition for surrounding rock. Note: R is the outer circle radius; r is the tunnel diameter.

Given that the stresses in Fig. 3b are axisymmetric, the expressions for radial and tangential stresses can be derived accordingly:

$$\begin{cases} \sigma_r = p \left(1 - \frac{r^2}{R^2} \right) = \frac{1}{2} (1 + \lambda) P_z \left(1 - \frac{r^2}{R^2} \right) \\ \sigma_\theta = p \left(1 + \frac{r^2}{R^2} \right) = \frac{1}{2} (1 + \lambda) P_z \left(1 + \frac{r^2}{R^2} \right) \end{cases} \quad (13)$$

The boundary conditions associated with Fig. 3c are as follows: (1) when $R = r$, $\sigma_r = \tau_{\theta r} = 0$; and (2) when $R \rightarrow \infty$, the expressions for σ_r and $\tau_{\theta r}$ can be derived according to Mohr–Coulomb strength theory:

$$\begin{cases} \sigma_r = -p' \cos 2\theta \\ \tau_{\theta r} = p' \sin 2\theta \end{cases} \quad (14)$$

Based on the aforementioned boundary conditions and the research outcomes of Cai et al.²¹, the stress in surrounding rock can be derived as follows:

$$\begin{cases} \sigma_r = -p' \left(1 - 4 \frac{r^2}{R^2} + 3 \frac{r^4}{R^4} \right) \cos 2\theta \\ \sigma_\theta = p' \left(1 + 3 \frac{r^4}{R^4} \right) \cos 2\theta \\ \tau_{\theta r} = p' \left(1 + 2 \frac{r^2}{R^2} - 3 \frac{r^4}{R^4} \right) \sin 2\theta \end{cases} \quad (15)$$

Integrating both scenarios leads to a total envelope stress solution represented as follows:

$$\begin{cases} \sigma_r = \frac{1}{2} (1 + \lambda) P_z \left(1 - \frac{r^2}{R^2} \right) - \frac{1}{2} (1 - \lambda) p_z \left(1 - 4 \frac{r^2}{R^2} + 3 \frac{r^4}{R^4} \right) \cos 2\theta \\ \sigma_\theta = \frac{1}{2} (1 + \lambda) p_z \left(1 + \frac{r^2}{R^2} \right) + \frac{1}{2} (1 - \lambda) p_z \left(1 + 3 \frac{r^4}{R^4} \right) \cos 2\theta \\ \tau_{\theta r} = \frac{1}{2} (1 - \lambda) p_z \left(1 + 2 \frac{r^2}{R^2} - 3 \frac{r^4}{R^4} \right) \sin 2\theta \end{cases} \quad (16)$$

According to Zhang et al.²³, the equations relating σ_r , σ_θ , and $\tau_{\theta r}$ to rock cohesion c can be obtained as follows:

$$\begin{cases} \sigma_r = \frac{1}{2} \left(1 + \frac{2c}{\sigma_c} \right) P_z \left(1 - \frac{r^2}{R^2} \right) - \frac{1}{2} \left(1 - \frac{2c}{\sigma_c} \right) p_z \left(1 - 4 \frac{r^2}{R^2} + 3 \frac{r^4}{R^4} \right) \cos 2\theta \\ \sigma_\theta = \frac{1}{2} \left(1 + \frac{2c}{\sigma_c} \right) p_z \left(1 + \frac{r^2}{R^2} \right) + \frac{1}{2} \left(1 - \frac{2c}{\sigma_c} \right) p_z \left(1 + 3 \frac{r^4}{R^4} \right) \cos 2\theta \\ \tau_{\theta r} = \frac{1}{2} \left(1 - \frac{2c}{\sigma_c} \right) p_z \left(1 + 2 \frac{r^2}{R^2} - 3 \frac{r^4}{R^4} \right) \sin 2\theta \end{cases} \quad (17)$$

The equations relating σ_r , σ_θ , and $\tau_{\theta r}$ to the internal friction angle φ can be derived as follows:

$$\begin{cases} \sigma_r = \frac{1}{2} \left[1 + \tan \left(\frac{\pi}{2} - \frac{\varphi}{2} \right) \right] P_z \left(1 - \frac{r^2}{R^2} \right) - \frac{1}{2} \left[1 - \tan \left(\frac{\pi}{2} - \frac{\varphi}{2} \right) \right] p_z \left(1 - 4 \frac{r^2}{R^2} + 3 \frac{r^4}{R^4} \right) \cos 2\theta \\ \sigma_\theta = \frac{1}{2} \left[1 + \tan \left(\frac{\pi}{2} - \frac{\varphi}{2} \right) \right] p_z \left(1 + \frac{r^2}{R^2} \right) + \frac{1}{2} \left[1 - \tan \left(\frac{\pi}{2} - \frac{\varphi}{2} \right) \right] p_z \left(1 + 3 \frac{r^4}{R^4} \right) \cos 2\theta \\ \tau_{\theta r} = \frac{1}{2} \left[1 - \tan \left(\frac{\pi}{2} - \frac{\varphi}{2} \right) \right] p_z \left(1 + 2 \frac{r^2}{R^2} - 3 \frac{r^4}{R^4} \right) \sin 2\theta \end{cases} \quad (18)$$

Numerical simulation

Model establishment

The numerical model is divided into two parts, where the structural components include the lining, segment, and grouting layer, while the solid components encompass various soil and rock layers. Adhering to St. Venant's principle as well as accounting for train loads and actual tunnel dimensions, the dimensions of the established 3D numerical mode were 60 m in length, 60 m in width, and 33 m in height, with 387,278 nodes and 268,800 elements. Normal constraints were applied to surrounding and bottom boundaries of the model. The 3D numerical model is displayed in Fig. 4. The soil and rock layers were simulated using solid elements. The physical and mechanical characteristics of soil and rock masses were identified through site investigation, as detailed in Table 1. Table 2 lists the materials properties for tunnel lining structure.

The Mohr–Coulomb model was selected for soil simulation, with a lower critical damping ratio applied during dynamic calculations. Hysteresis damping was taken as a default value, while Rayleigh damping was set to be a critical damping ratio of 0.5%. The existing tunnel lining structure, the new shield segment, and the grouting layer were all modelled with elastic elements.

The newly constructed shield tunnel was excavated incrementally at 1.5 m per cycle. Considering the length and weight of the shield, an elastomer model was employed for the shield shell, and its density and elastic modulus were assigned based on actual engineering practices. The chamber pressure was simulated by applying surface loads to the tunnel face. The grouting pressure was modelled by radial loads applied to the surrounding soil. The friction force was modelled by applying transverse loads to the soil surrounding the shield shell. The thrust force was simulated by applying nodal forces to the segment elements. According to the calculation formula, the friction force is not uniformly distributed on the contact surface between the shield shell and the

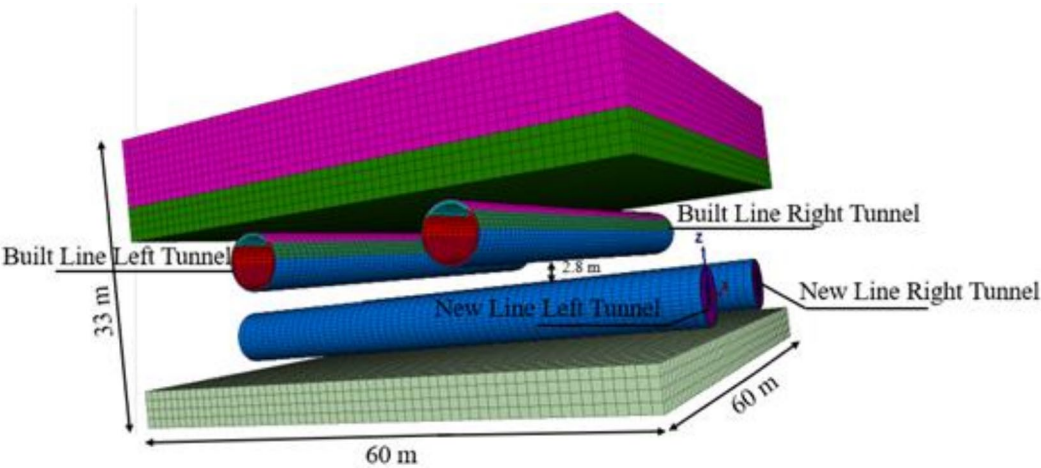


Fig. 4. Numerical model.

Strata	Natural density (g/cm ³)	Cohesion (KPa)	Angle of internal friction (°)	Poisson's ratio	Bulk modulus (MPa)	Elastic modulus (MPa)
Cohesive fill soil	1.97	15	12	0.35	3.5	9.3
Silty clay	1.95	35	15	0.33	4.6	12
Highly weathered mudstone siltstone	2.12	40	27	0.28	65.2	200
Moderately weathered mudstone siltstone	2.72	200	30	0.25	986	3000

Table 1. Physical and mechanical properties of the strata.

Materials	Densities (g/cm ³)	Poisson's ratio	Bulk modulus (MPa)	Modulus of elasticity (MPa)	Shear modulus (MPa)
Primary support	2.45	0.167	10,700	25,000	16,200
Secondary lining	2.5	0.167	12,860	30,000	16,200
Segment	2.5	0.2	15,300	27,600	11,500
Grout equivalent circle zone	2.3	0.25	450	1200	800

Table 2. Physical and mechanical properties for structural materials.

soil; instead, the friction force magnitude at each point depends on the coordinates and angle associated with that point. Therefore, this study employed the built-in Fish language in FLAC3D to apply relevant loads to the soil in contact with the shield shell, where angle and coordinates were utilized as variables. This approach aimed to simulate the effect of friction on the soil and enhance the accuracy of numerical calculations while ensuring that the results align more closely with actual engineering conditions.

Details of numerical simulation

Given the minimal impact of groundwater at the construction site, groundwater seepage effect was not considered. The numerical simulation consisted of the following procedures:

- 1. Develop a numerical model of the foundation pit.
- 2. Disable the dynamic analysis mode, assign soil parameter values to the model, and perform equilibrium calculation for the foundation pit under initial gravitational conditions.
- 3. Excavate the tunnel in stages and conduct stress equilibrium calculations after each excavation stage.
- 4. Apply both static and dynamic loads from trains to the railway foundation of the existing tunnel, followed by displacement calculations under various loading conditions.

Setup of monitoring points

The region most affected by shield tunneling is typically located between the left and right lines of the new tunnel. The second most affected region is usually situated at the intersection of the new and existing tunnels. Consequently, the layout of the monitoring points are illustrated in Fig. 5.

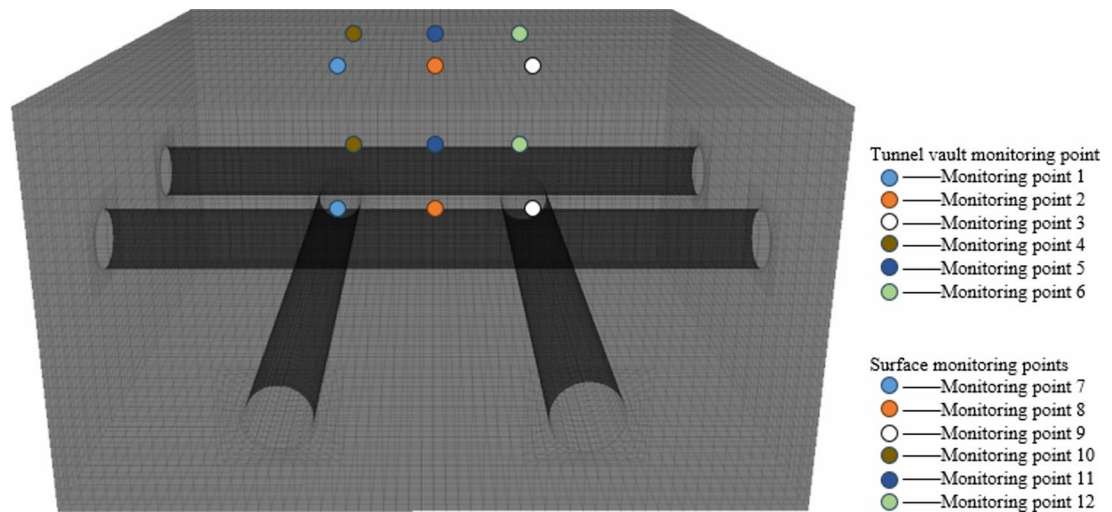


Fig. 5. Layout of monitoring points.

Analysis of computational results

Impact on displacement before and after application of dynamic loads

Figure 6 compared the vault displacements for the existing tunnel under conditions with and without dynamic loads applied at 80 km/h. It was revealed that the maximum uplift differences were 5.2 mm and 7.0 mm, respectively, while the horizontal displacement differences were 2.2 mm and 2.26 mm, respectively. After the application of dynamic loads, displacement increased significantly, which was primarily attributed to geological conditions, softening of the strata from the dynamic load, as well as the durations of friction, chamber pressure, and grouting pressure during excavation.

Since the shield tunneling first passed through the left line of the existing tunnel and then the right line, the friction, chamber pressure, and grouting pressure on the left and right lines varied over time. The deformation curves for these two lines differed and exhibited different variation trends. The peak uplifts at the arch of the existing tunnel's left and right lines before and after applying the dynamic load were approximately 3.0 mm and 3.1 mm, respectively. The horizontal displacement of the existing tunnel under both conditions increased as cutterhead approached, and then gradually stabilized after the shield tail passed. The maximum deformation differences between the two conditions were small, with values at six monitoring points on vault being 1.14, 1.03, 1.02, 1.05, 0.98, and 1.10 mm, respectively. The time needed for tunnel deformation to stabilize varied, where the horizontal deformations of the left and right lines stabilized after approximately 25 and 40 excavation cycles, respectively.

Impact of dynamic loads on displacements

Numerical simulations were conducted under four conditions: no train load, 40 km/h train load equivalent to static soil pressure (static load), 40 km/h dynamic load, and 80 km/h dynamic load. Figure 7 illustrates the results from measuring point 1. The displacement curves for static load and 40 km/h dynamic load were almost identical, demonstrating similar increasing rates. In this case, the application of dynamic loads minimally affected the lateral displacements. Thus, for train speeds of 40 km/h or less, the train load can be treated as equivalent to a static load for analysis purposes.

Stress evaluation in the rock surrounding the tunnel.

Figure 1 revealed that the strata near the centreline of the existing tunnel transition from silty clay to strongly weathered muddy siltstone, and then to moderately weathered muddy siltstone. At this stage, as described in section "Stress in surrounding rock of existing tunnels", lithological changes around the upper tunnel resulted in variations in rock cohesion c and internal friction angle φ . Consequently, the σ_θ and σ_r magnitudes that the surrounding rock can withstand also changed. In addition, the dynamic loads from trains in the tunnel could easily cause the surrounding strata to fail first.

Derivations from Eqs. (10) to (18) indicated that as the stratum around the upper tunnel transitions from homogeneous hard rock to homogeneous soft rock, both c and φ gradually decrease. Consequently, the radial stress σ_r and the tangential stress σ_θ also decreased, which indicated a higher stress release rate in soft rock surrounding the upper tunnel. Specifically, the vault settlement was more affected by σ_r . A higher stress release rate corresponded to greater settlement caused by excavation of the lower tunnel and dynamic loads from the train in the upper tunnel.

This analysis suggested that the stress distribution within the surrounding rock of the upper tunnels significantly differs from that within a uniform stratum. This discrepancy was evident as the stress release in soft rock was significantly higher than that in hard rock. Therefore, at the same location, stress values in soft rock were lower than those in hard rock. This resulted in an uneven stress distribution within the surrounding rock, leading to plastic and deformation zones primarily located in the surrounding rock with poorer properties.

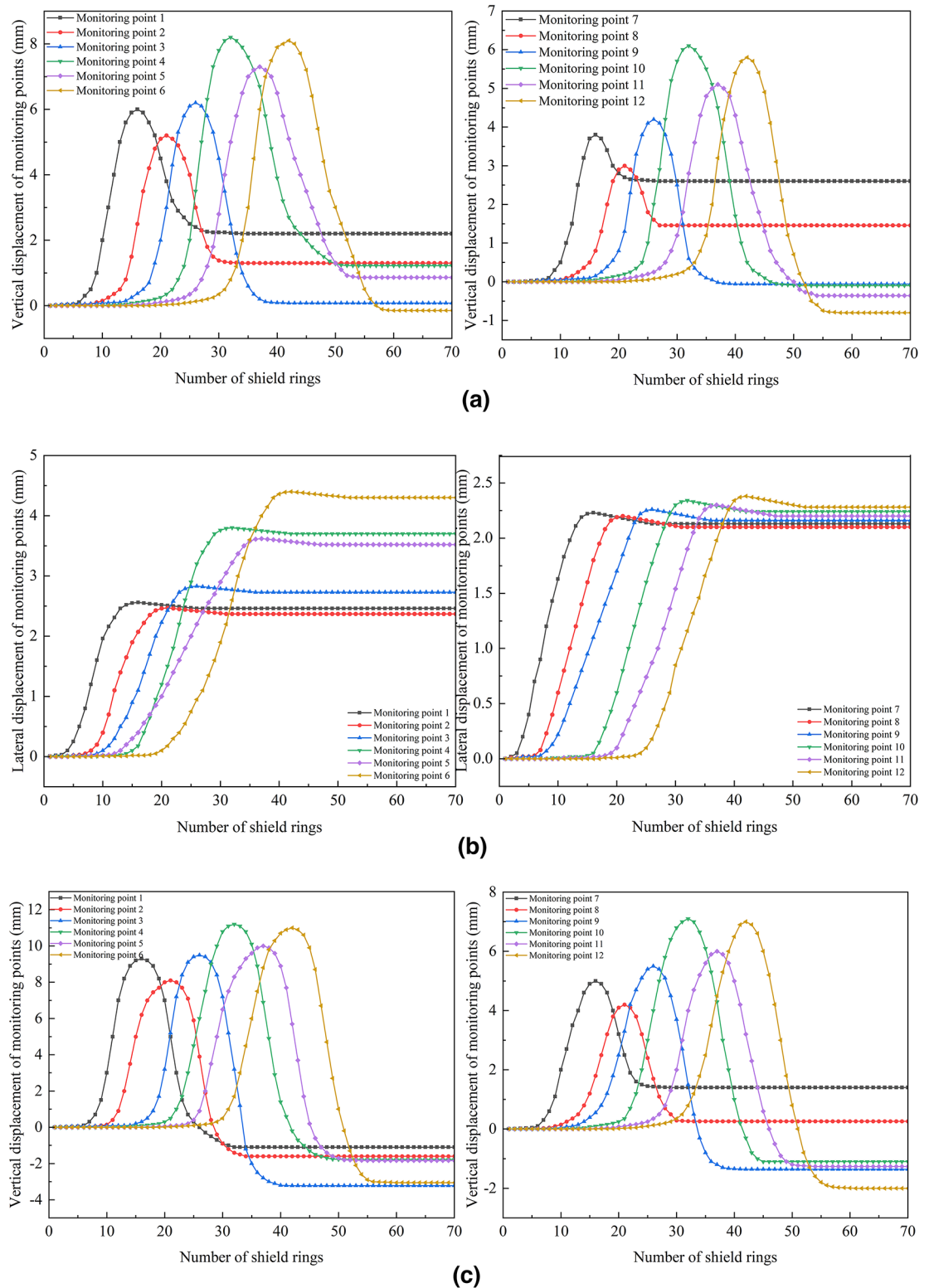


Fig. 6. Displacement curves at various monitoring points.

As illustrated in Fig. 8, as the interface between soft and hard rock rotated counterclockwise around the tunnel center, the angle between the interface and the horizontal line, denoted as α , ranged from 0° to 90° . As α increased, the rock on the left side of the vertical line gradually transitioned to soft rock, resulting in a higher proportion of soft rock in the surrounding rock of the left tunnel. According to Eqs. (17) and (18), the stresses in the surrounding rock of the left tunnel easily reached its limit. Once the stress release rate limit was exceeded, the upper tunnel on the left side sustained damage, with the left surrounding rock being the first

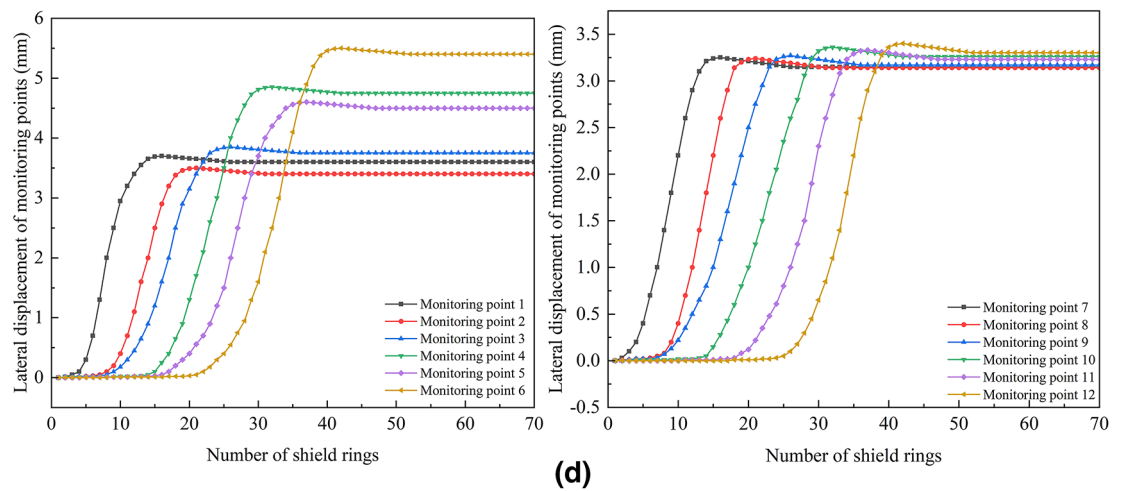


Figure 6. (continued)

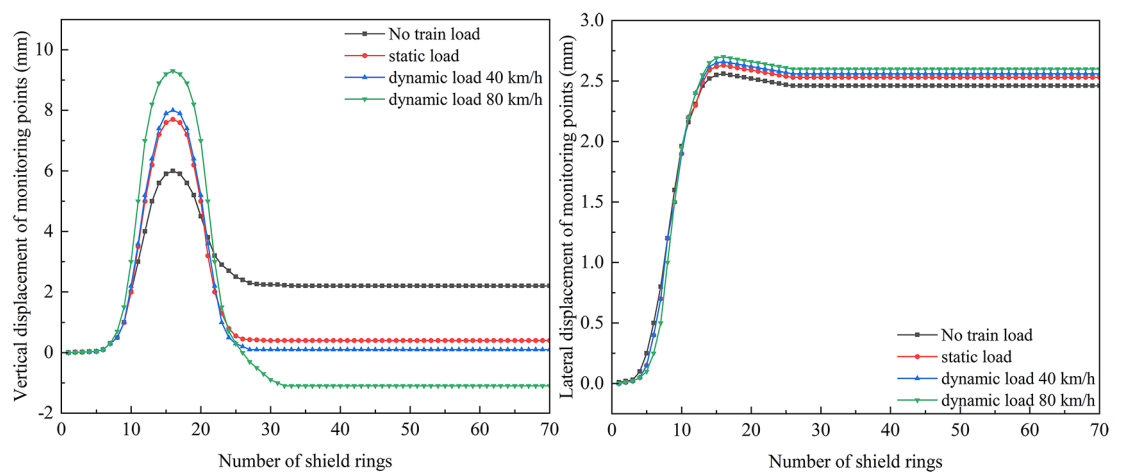


Fig. 7. Displacement curves at monitoring point 1 under different dynamic load conditions.

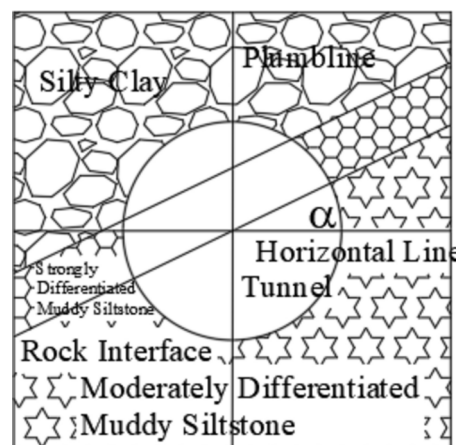


Fig. 8. Stratigraphic distribution of the upper tunnel.

Working condition		Vertical displacement/mm	Lateral displacement/mm	Safety and stability coefficient
Load pattern	Speed/km/h			
No	No	8.2	4.4	1.526
Static load	40	9.3	4.7	1.436
Dynamic load	40	9.7	4.9	1.431
Dynamic load	80	11.1	5.4	1.419
Actual measured value		10.3	5	–

Table 3. Comparison between measured data and maximum simulation values.

to fail. Subsequently, new loads developed on the right side, leading to the failure of the right surrounding rock. In practical engineering, deformation at the soft-hard rock interface must be monitored to prevent similar structural failures.

Discussion

Considering the extensive computational demands for assessing model stability, FLAC3D software and strength reduction method were employed to determine the safety stability coefficients across various operational conditions. Table 3 summarizes the numerical results.

It was observed that when using the proposed model, which accounts for dynamic loads, the simulation errors relative to actual measured values were 0.8 and 0.4 mm, respectively, which were 1.3 and 0.2 mm lower than those of the model without considering dynamic loads. This observation demonstrated the accuracy of the proposed simulation approach. At a train speed of 80 km/h, the maximum vertical displacement at the monitoring point was 11.1 mm, indicating an increase of 2.9 mm relative to the situation without dynamic load. The safety and stability coefficient in this case was 1.419, which fell within the standard range. When trains travel at 40 km/h, the predicted overall responses were comparable under both static and dynamic load conditions. Thus, train speeds of 40 km/h or less can be considered equivalent to static loads for analysis purpose. In summary, the effect of dynamic load on mechanical behavior should be thoroughly considered in construction projects. Ignoring this issue may lead to deviations in the safety and stability coefficients and pose a serious threat to the safety of nearby projects and metro operations, which warrants attention.

Conclusions and recommendations

Excavation of adjacent shield tunnels has always been a challenging problem that is affected by dynamic loads from existing tunnels, groundwater, ground subsidence, and ground fissures. This study utilized existing deformation data from a comparable project to develop a simulation method for shield-soil friction under dynamic load conditions during excavation of new tunnels. Based on the analysis of surrounding rock stress and strength reduction method, this study revealed the relationship between the dynamic loads from subway trains and the tunnel stability. The following conclusions are drawn:

1. The numerical models that considers the combined effects of dynamic loads and friction surrounding the shield were developed using the FLAC3D software to more accurately depict the impact of tunnel excavation on nearby existing tunnels. Under a dynamic load condition, the overall safety and stability coefficient decreased by approximately 0.1 compared to the condition without train load. It is essential to carefully consider the impact of dynamic train loads on the overall structural stability of the surrounding region when excavating new adjacent tunnels.
2. The dynamic train load can be considered equivalent to a static load for analysis purposes, while the premise is that the train's speed does not exceed a certain threshold.
3. The stress distribution within the surrounding rock of the upper tunnels significantly differed from that within a uniform stratum. This difference was reflected by the fact that the stress release in soft rock was significantly higher than that in hard rock. Thus, an uneven distribution of surrounding rock stress occurred, which resulted in plastic and deformation zones surrounding the upper tunnel mainly concentrated in the surrounding rock with poorer properties.
4. As the interface between soft and hard rock rotated counterclockwise around the tunnel centre, the stress that the surrounding rock of the tunnel on the left side of the vertical line can withstand may easily reach its limit. When the space between the upper and lower tunnels was insufficient, sensitivity to disturbances from train loads. Reducing train speed could minimize the interference with the construction process.
5. The proposed simulation approach in this study did not consider the impacts of factors such as groundwater and surface structures. As a result, there were still discrepancies between calculated results and observed measurements. It is recommended that future research should provide a more comprehensive and detailed analysis of the aforementioned factors.

Data availability

Data is provided within the manuscript or supplementary information files.

Received: 14 September 2024; Accepted: 25 November 2024
Published online: 11 March 2025

References

1. Liu, Y. N. et al. Three-dimensional stability analysis of shield tunnel face adjacent to existing tunnels. *Chin. J. Geotech. Eng.* **45**(7), 1374–1383. <https://doi.org/10.11779/CJGE20220439> (2023) (in Chinese).
2. Zhang, B. & Sun, Q. L. Upper bound analysis of the anti-seismic stability of slopes considering the effect of the intermediate principal stress. *Front. Earth Sci.* **10**, 01–11. <https://doi.org/10.3389/feart.2022.1023883> (2023).
3. Lou, P. & Li, T. Research on the influence of shield tunneling on the ground settlement in overlapping metro tunnels. *Journal of Railway Engineering Society* **09**, 66–71 (2020) (in Chinese).
4. Zhu, C. G. et al. Time series multi-sensors of interferometry synthetic aperture radar for monitoring ground deformation. *Front. Environ. Sci.* **10**, 3389–3401. <https://doi.org/10.3389/fenvs.2022.929958> (2022).
5. Ding, Z. et al. Numerical analysis of influence of shield tunnel in soft soil passing over existing nearby subway. *J. Central South Univ. (Sci. Technol.)* **03**, 663–671. <https://doi.org/10.11817/j.issn.1672-7207.2018.03.020> (2018) (in Chinese).
6. Zhou, J. et al. Enhancing the performance of tunnel water inflow prediction using Random Forest optimized by Grey Wolf Optimizer. *Earth Sci. Inform.* **16**(3), 2405–2420. <https://doi.org/10.1007/s12145-023-01042-3> (2023).
7. Zou, J. F., Chen, G. H. & Qian, Z. H. Tunnel face stability in cohesion–frictional soils considering the soil arching effect by improved failure models. *Comput. Geotechn.* **106**, 1–17. <https://doi.org/10.1016/j.compgeo.2018.10.014> (2019).
8. Li, S. Q. et al. Analysis of bearing structures around deep soft rock roadway. *Disaster Adv.* **06**, 250–255 (2013).
9. Lu, D. Y. et al. Research on effects of new shield tunnel on longitudinal deformation of existent tunnel. *J. China Railw. Soc.* **10**, 108–116. <https://doi.org/10.3969/j.issn.1001-8360.2016.10.015> (2016) (in Chinese).
10. Long, S. C. et al. Solid model bridge static damage monitoring based on GBSAR. *J. Geodesy Geoinf. Sci.* **5**(4), 38–49. <https://doi.org/10.11947/j.jggs.2022.0404> (2022).
11. Wang, X. R. et al. Vibration response caused by silt layer in underground subway under small radius curve tunnel. *Earth Sci.* **48**(6), 2415–2426. <https://doi.org/10.3799/dqkx.2023.063> (2023) (in Chinese).
12. Xiang, M. L. et al. Failure mechanism analysis of prestressed anchor cable treatment for tunnel bottom heave under train dynamic load. *J. Vib. Shock* **42**(15), 190–198. <https://doi.org/10.13465/j.cnki.jvs.2023.15.023> (2023) ((in Chinese)).
13. Li, M. et al. The variation of micro-current in rock under loads and its microcosmic influence mechanism. *Eng. Geol.* **310**(5), 106877. <https://doi.org/10.1016/j.enggeo.2022.106877> (2022).
14. Long, S. C. et al. Health monitoring and safety evaluation of bridge dynamic load with a ground-based real aperture radar. *Surv. Rev.* **54**(383), 172–186. <https://doi.org/10.1080/00396265.2021.1920792> (2022).
15. Liu, W. Z. et al. Influences of vibration load of elevated subway train on the stress and deformation of adjacent structures. *Adv. Eng. Sci.* **6**, 97–108. <https://doi.org/10.15961/j.jsuese.202200462> (2023).
16. Ma, Z. Analysis of the dynamic response of train loads on adjacent subway structures. *J. Wuhan Univ. Technol. Transp. Sci. Eng.* **41**(1), 109–118. <https://doi.org/10.3963/j.issn.2095-3844.2017.01.021> (2017).
17. Chen, H. et al. Analysis of the influence of train dynamic load on the stability of adjacent foundation pit. *Earthq. Eng. Eng. Dyn.* **42**(5), 168–174. <https://doi.org/10.13197/j.eeed.2022.0518> (2022) (in Chinese).
18. Wu, H. G. & Guan, W. Research on the progress of dynamic response of pile-soil composite foundation under train load. *J. Railw. Eng. Soc.* **39**(7), 1–11 (2022) (in Chinese).
19. Zheng, C. J. et al. Analytical solution for dynamic interaction of end-bearing pile groups subjected to vertical dynamic loads. *Chin. J. Geotech. Eng.* **44**(12), 2187–2195 (2022) (in Chinese).
20. Yin, M. L. et al. Effect of the excavation clearance of an under-crossing shield tunnel on existing shield tunnels. *Tunnel. Undergr. Space Technol.* **78**, 245–258. <https://doi.org/10.1016/j.tust.2018.04.034> (2018).
21. Cai, M. F. *Geotechnical Mechanics and Engineering* (Science Press, Beijing, 2002).
22. Zhao, Y. & Liu, H. H. An elastic stress-strain relationship for porous rock under anisotropic stress conditions. *Rock Mech. Rock Eng.* **45**(3), 389–399. <https://doi.org/10.1007/s00603-011-0193-y> (2012).
23. Zhang, N. X. et al. Study of relationship between Poisson's ratio and angle of internal friction for rocks. *Chin. J. Rock Mech. Eng.* **30**(s1), 2599–2609 (2011) (in Chinese).

Author contributions

Hao Li wrote the main manuscript text and prepared Figures. Jian Zhou prepared tables. Sichun Long supervised the whole project and edited the manuscript. All authors reviewed the manuscript.

Funding

The National Natural Science Foundation of China (Nos.42377453; 41877283); The Science and Technology Innovation Program of Hunan Province (Nos.2021RC4037;2023JJ30235); Scientific Research Project of Hunan Provincial Department of Natural Resources (No.2021-18).

Competing interests

The authors declare no competing interests.

Additional information

Supplementary Information The online version contains supplementary material available at <https://doi.org/10.1038/s41598-024-81128-0>.

Correspondence and requests for materials should be addressed to S.L.

Reprints and permissions information is available at www.nature.com/reprints.

Publisher's note Springer Nature remains neutral with regard to jurisdictional claims in published maps and institutional affiliations.

Open Access This article is licensed under a Creative Commons Attribution-NonCommercial-NoDerivatives 4.0 International License, which permits any non-commercial use, sharing, distribution and reproduction in any medium or format, as long as you give appropriate credit to the original author(s) and the source, provide a link to the Creative Commons licence, and indicate if you modified the licensed material. You do not have permission under this licence to share adapted material derived from this article or parts of it. The images or other third party material in this article are included in the article's Creative Commons licence, unless indicated otherwise in a credit line to the material. If material is not included in the article's Creative Commons licence and your intended use is not permitted by statutory regulation or exceeds the permitted use, you will need to obtain permission directly from the copyright holder. To view a copy of this licence, visit <http://creativecommons.org/licenses/by-nc-nd/4.0/>.

© The Author(s) 2024